Journal of Cleaner Production 400 (2023) 136688

Contents lists available at ScienceDirect

Journal of Cleaner Production

journal homepage: www.elsevier.com/locate/jclepro

Analysis and modelling of single domain core-shell (αFeNi/chromite) nanoparticles emitted during selective laser melting, and their magnetic remanence

Richard Dvorsky [a,b,*], Jana Kukutschová [b], Marek Pagáč [c], Ladislav Svoboda [a], Zuzana Šimonová [a,c,d], Kateřina Peterek Dědková [b,e], Jiří Bednář [a], Rafael Gregorio Mendes [f], Dalibor Matýsek [e], Ondřej Malina [g], Jiří Tuček [h], Zuzana Vilamová [a,i], Sergei Kiselev [i], Thomas Gemming [f], Peter Filip [j]

[a] Nanotechnology Centre, CEET, VSB – Technical University of Ostrava, 17. listopadu 15/2172, Ostrava, 708 00, Czech Republic
[b] Faculty of Material Science and Technology, Center for Advanced Innovation Technologies, VSB – Technical University of Ostrava, Ostrava, 17. listopadu 15/2172, Ostrava, 708 00, Czech Republic
[c] Department of Machining, Assembly and Engineering Metrology, Faculty of Mechanical Engineering, VSB – Technical University of Ostrava, 17. listopadu 15/2172, Ostrava, 708 00, Czech Republic
[d] IT4Innovations, VSB – Technical University of Ostrava, 17. listopadu 15/2172, Ostrava, 708 00, Czech Republic
[e] Faculty of Mining and Geology, VSB – Technical University of Ostrava, Ostrava, 17. listopadu 15/2172, Ostrava, 708 00, Czech Republic
[f] Leibniz Institute for Solid State and Materials Research Dresden, Helmholtzstraße 20, 01069, Dresden, Germany
[g] Regional Centre of Advanced Technologies and Materials, Czech Advanced Technology and Research Institute (CATRIN), Palacký University Olomouc, Křížkovského 511/8, 779 00, Czech Republic
[h] Department of Mathematics and Physics, Faculty of Electrical Engineering and Informatics, University of Pardubice, Studentská 95, 530 02, Pardubice, Czech Republic
[i] Faculty of Material Science and Technology, VSB – Technical University of Ostrava, Ostrava, 17. listopadu 15/2172, Ostrava, 708 00, Czech Republic
[j] Southern Illinois University at Carbondale, Carbondale, IL, 62901, USA

ARTICLE INFO

Handling Editor: Panos Seferlis

Keywords:
Additive manufacturing
Core-shell nanoparticles
Kamacite
Superparamagnetism
3D printing
316L Stainless steel

ABSTRACT

Despite recent intense implementation of increasingly eco-friendly additive manufacturing, the properties of nanoparticulate pollutants emitted during Laser Powder Bed Fusion are still not fully understood, and have generally been overlooked. This study aims to fill this gap in current research by providing new insights into distinct metal/oxide core-shell nanoparticles (3–36 nm) that are produced during 3D printing using stainless steel. It also suggests possible ways for the removal of these potentially harmful by-products. Further, this research also provides a newly developed kinetic model that predicts a metal core growth time of below 200 μs and confirms the predicted theory for the formation of these by-products. In the current study it was found that the cores produced during this process are purely metallic and consist of meteoroid phase kamacite (αFeNi). Within this study there was found to be a complete dominance of single-domain cores of kamacite with prevailing particles below the superparamagnetic threshold showing strong magnetic response and remanence. This new knowledge can be used to minimize potential health risks and reduce contamination of raw materials by this nanoparticulate pollutant, which can adversely affect the quality of printed metal parts, the environment, and the health of the operator. These findings also provide a new possibility of targeted efficient production of superparamagnetic core-shell nanoparticles with a metallic kamacite core during laser powder bed fusion of austenitic steel 316L powder, which can be used in the production of sensors.

1. Introduction

Additive manufacturing (AM) is considered to be an emerging technology within Industry 4.0 which has the potential to enable companies to produce complex products and components in a more efficient and sustainable way (Hu et al., 2020; Wu et al., 2022). Currently, AM

* Corresponding author. Nanotechnology Centre, CEET, VSB – Technical University of Ostrava, 17. listopadu 15/2172, Ostrava, 708 00, Czech Republic.
E-mail address: richard.dvorsky@vsb.cz (R. Dvorsky).

https://doi.org/10.1016/j.jclepro.2023.136688
Received 14 June 2022; Received in revised form 1 March 2023; Accepted 4 March 2023
Available online 6 March 2023

can be used to create objects using various materials, from organic polymers to metallic powders, which can then be used in the manufacturing process of many different products (Lin et al., 2019; Wang et al., 2018). It has been found that according to a Life Cycle Assessment (LCA), AM of metal parts reduces their environmental impact (Huang et al., 2016). Austenitic steel 316L is the second most commonly used material in AM, after 304L, and is the most common structural material used, with a wide range of applications in the engineering, food, medical devices, automotive, aerospace, and petroleum industries (Calignano et al., 2017; Harun et al., 2018).

Recent papers have mostly been focused on the whole green product life cycle management of different metal parts such as aircraft engine turbine blades, or metal engine parts in light distribution trucks (Böckin and Tillman, 2019; Torres-Carrillo et al., 2020), or on optimising the additive manufacturing process and improving the quality of the final product (Kanyilmaz et al., 2022; Liu et al., 2018) without studying the by-products of the 3D printing process itself. However, it is already known that Laser Powder Bed Fusion (LPBF), like welding, generates emissions which may cause particulate air pollution that in turn can create risks to occupational health (Berlinger et al., 2011; Chen et al., 2020; Ko et al., 2021). Very few studies have reported the presence of unintentionally formed nanoparticles whilst dealing with powdered stainless steel LPBF (Gasper et al., 2018; Noskov et al., 2020, 2022). However, recently Noskov et al. studied nanoparticles emitted during laser additive manufacturing with stainless steel powder using transmission electron microscopy, where they also performed analysis of individual nanoparticles using scanning transmission electron microscopy with a high-angle annular dark field detector (HAADF STEM). This study confirmed the core-shell structure of the nanoparticles, which consisted of Fe, Cr and Ni atoms and an oxide shell layer (Noskov et al., 2022).

Although AM is generally considered to be environmentally friendly, during LPBF nanoparticles of metal vapor condense above the laser melt pool and expand into the surrounding chamber space, where they are deposited on the walls and instrument optics. This staining of the optical elements in a laser system can influence the quality of the laser beam and thus the quality of the final products (Murzin, 2022; Sun et al., 2021). Once coated these lenses have to be decontaminated by opening the chamber, generally by mechanical means, which can significantly damage the operator's respiratory tract. It is also known that one of the most dangerous substances is this nanoparticle condensate, which is formed by the evaporation of liquid metal and condensation in the form of fine particles with a high surface area in the filter, making filter replacement the most dangerous part of 3D printer operation (DebRoy et al., 2019; Hu et al., 2020).

This by-production of these unwanted nanoparticle emissions with potentially negative environmental and human health impacts needs to be addressed to further develop LPBF as a clean processes within sustainable engineering. A deeper understanding of the physico-chemical properties of these emissions can contribute to a better understanding of health and safety risks at work, and can lead to the possible reduction or the complete elimination of this type of pollution.

This study describes the formation of spherical nanoparticles that form directly above the laser melt pool in buoyancy at reduced inert gas pressure and opens for the first time new possibilities for the targeted preparation of core-shell superparamagnetic nanoparticles using LPBF-based techniques. At present active preparation of metal nanoparticles is often used by trapping emissions from the laser ablation process into the liquid medium above the surface, during which possible deformations due to cavitation implosions may occur (Hu et al., 2020). None of the above mentioned works have tackled a detailed phase analyses of the by-product material formed, analyzed detailed high-resolution transmission electron microscopy (HRTEM) images of the individual core-shell particles, dealt with the mathematical modelling of the mechanism of nanoparticle formation or their magnetic properties, which this paper to address. In addition to this, a kinetic model for the formation and growth of nanoparticles of the by-product was derived, confirming the mode of formation of this by-product.

This study aims to fill current research gaps and to verify whether the emitted, harmful aerosol contains particles with such properties that would allow them to be captured by magnetic separation or other means, thus allowing for cleaner, safer AM of austenitic steel 316L powder.

2. Experimental and simulation methods

2.1. Materials and conditions of 3D printing

The studied particulate material (Fig. 1A) was created from primary stainless steel powder 316L-0407 (DIN 1.4404) (RENISHAW, 2018) during the operation of a 3D laser printer (Renishaw AM400) and collected from the surface of the inner walls of the working chamber. The periodic heating regime of the relevant area of the primary metallic material was realised by a pulsed ytterbium fiber laser 350 W (focus size $\approx$ 70 μm) at a pulse length of 80 μs. The protective gas in the printing chamber was Argon 5.0 (purity $\geq$99.999%) with a pressure of 13 mbar and with an O_2 content <2 ppm and H_2O < 2 ppm. Its forced circulation (gas flow) with a flow rate of about 0.7 m s^{-1} was above the print plane.

2.2. Method of materials collection

The powdered material of deposited condensate nanoparticles, which were extracted from the inner walls of the chamber with a fine brush, were contaminated with primary 316L austenitic steel microparticles during the process. For further study, these large primary particles were separated by sedimentation from the rest of the fine condensate fraction. To ensure that the nature of the metal/oxide material was not affected by hydration in aqueous media, sedimentation was carried out in acetone. Fine liquid nanodispersion was then used for size measurements by dynamic light scattering (DLS). Dry nanopowder for further analyses was subsequently obtained by the evaporation of acetone. This is a new and different approach to obtain a large amount of nanoparticle by-products of good quality and quantity. In other works, the nanoparticualte by-products were obtained through air sampling via direct sedimentation on TEM grids during 3D printing under typical working conditions. Following this a particle size distribution histogram is usually obtained by counting particles from several TEM images (Noskov et al., 2022). This methodology was also performed and included in this paper (Fig. S1). However, in this study, the particle size distribution histogram was enhanced by measuring the core size of several core-shell particles from HRTEM images (Fig. S2). Similar to (Noskov et al., 2022), the evaporated material was then captured and collected on TEM grids for further characterization. Conversely, Gasper et al. dealt with much larger particles with particle sizes in the range of 1–273 μm (Gasper et al., 2018).

Additionally, instead of the more commonly used elemental point mapping used in previous studies, the method used in this study provided more detailed information on the representation of individual elements on the radial line of the core-shell nanoparticle by using quantitative linear scanning transmission electron microscopy elemental analysis.

2.3. Methods of material characterization

For images a JEOL 2200FS (JEOL, Ltd., Japan) HRTEM equppied with 200 kV field emission electron gun + energy filtering transmission electron microscope (EF-TEM), an electron energy loss spectroscope using an in-column filter (EELS), an energy-dispersive X-ray spectroscope (EDX), and a scanning transmission electron microscope (STEM) was used.

Powder X-ray diffraction analyzes were carried out using a Bruker-AXS D8 Advance instrument (BRUKER, Germany) with a 2Q/Q

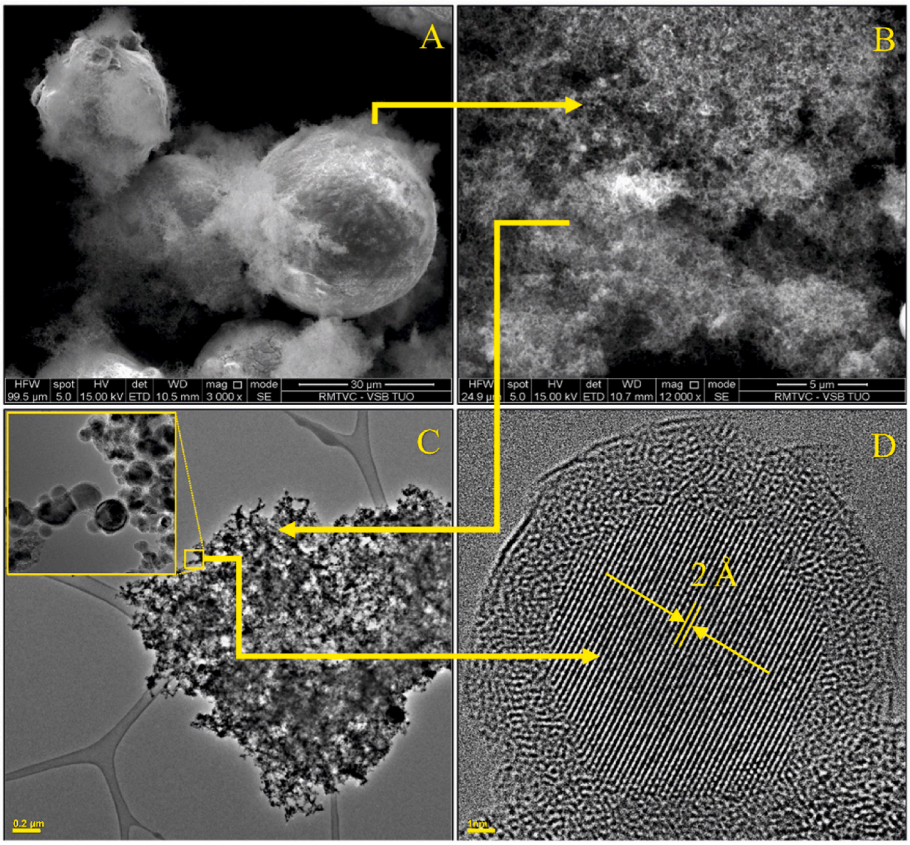

Fig. 1. Morphology of newly formed nanoparticles. (**A**) SEM image of newly formed nanoparticle aggregates attached to the surface of globular microparticles of primary metal material (Stainless Steel 316L). Scale bar, 30 μm. (**B**) Detailed image of this aggregate. Scale bar, 5 μm. (**C**) TEM image of the nanoparticle aggregate. Scale bar, 0.2 μm. (**D**) HRTEM image of nanoparticle core-shell structure. Scale bar, 1 nm.

measurement geometry and the positionally sensitive detector LynxEye under the following conditions: CuK/Ni-filtered radiation, voltage 40 kV, current 40 mA, step mode with a step of 0.014° 2Q, total time 25 s per step and angular extent 5–80° 2Q.

The mineral observation and microanalyses were carried out on an electron microscope FEI Quanta 650 FEG (FEI Company, USA), with EDX, wide distribution analysis (WDA), and electron backscatter diffraction (EBDS) detectors made by EDAX and a cathodoluminescence (CL) detector Mono 4 made by Gatan (USA). Analytical conditions were as follows: 15 kV beam voltage, 8–10 nA current, 4–6 μm beam diameter, and a vacuum ~20 Pa.

The given values of the individual metal fractions were also verified by elemental analysis by using inductively coupled plasma-atomic emission spectrometry (ICP-AES) (Spectro Arcos, Germany).

Analysis of particle size distribution was performed by a dynamic light scattering (DLS) method using a Malvern Zetasizer Nano ZS (Malvern Instruments Ltd, UK) equipped with a 4 mW/633 nm laser.

Samples were analyzed using a Physical Properties Measurement System (PPMS DynaCool system) (Quantum Design, USA) with the vibrating sample magnetometer (VSM) option. The experimental data were corrected for the diamagnetism and the signal of the sample holder. The temperature dependence of the magnetization was recorded in a sweep mode of 1 K/min in the zero-field-cooled (ZFC) and field-cooled (FC) measuring regimes from 5 to 300 K at a given external magnetic field of 1000 Oe. The hysteresis loops were recorded at a temperatures of 5 and 300 K in externally magnetic fields ranging from –50 kOe to +50 kOe.

3. Results and discussion

Fig. 1 shows large aggregates of globular core-shell nanoparticles with dimensions much smaller than 100 nm. These aggregates were formed from metal vapors above the melting pool during the condensation and solidification throughout 3D printing process. While a small part of these emissions remains bound to the globular particles of the primary material in the immediate vicinity of the melting pool (Fig. 1A), the majority are carried away by a circulating shielding gas and deposited on the gas filter and parts of the working chamber. The particulate material for our experiments was obtained by collecting from these areas.

The detail of the TEM image of emitted particles (Fig. 1C) confirmed the dominant proportion of particles with dimensions below 100 nm. The individual nanoparticles have a predominantly globular shape Fig. 2A and their statistical size distribution Fig. 2B shows a mean value of 14 nm in diameter (Fig. S1). The subsequent detailed HRTEM analysis of relatively more isolated nanoparticles revealed a clear core-shell structure. Dimensional analysis of a set of 30 clearly visible core-shell nanoparticle structures (Fig. 2A) shows that the ratio of the diameters of the globular core (d_{core}) and the shell (d_{shell}) corresponds to the mean value of 0.679 with the correlation of R = 0.9642 ($d_{core} = 0.679 \bullet d_{shell}$) – (Fig. S2). Based on this reasonable approximation of the independence of this ratio of absolute particle size, the core size distribution was mathematically derived (Fig. 2B). The mean value of the core diameter in this derived distribution is 9.5 nm.

Several HRTEM images show a clear crystalline structure in the core (Fig. 1D), in contrast to the shell, which exhibits a very vague structure. Lattice spacing Fast Fourier Transform (FFT) analysis of selected HRTEM images (Fig. 2A) with a clear crystal structure (Fig. S3) gave a value of

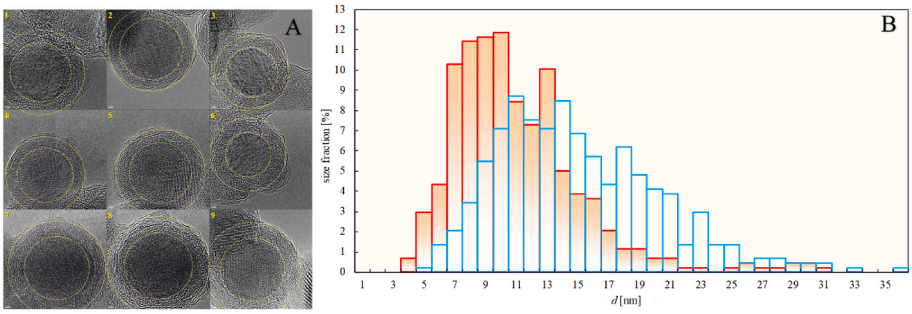

Fig. 2. Morphology and size distribution of individual core-shell nanoparticles. (**A**) Selected HRTEM images of nanoparticles with evident core-shell structure. (**B**) Primary statistical distribution of overall core-shell nanoparticle sizes obtained by image analysis −− (Fig. S1) and derived core size distribution −− (Fig. S2).

the resulting interplanar distance ($d_1 = 2.03 \pm 0.02$ Å). With regard to the composition of the primary metallic material, this value is hypothetically similar to some phases from the binary system (Fe, Ni) (Table 1) (Barthelmy, 2021).

The question is whether the hypothesis of complete dominance of iron (nickel-enriched) in the core can be supported by measured results. By elemental mapping in STEM mode along the radial axis of the analytical field (Fig. 3 - left), parallel profiles of the Fe, Ni, Cr and O in relative units were created (Fig. 3 - right).

The measured proportions of chromium and oxygen is approximately uniform along the entire radial line of the core-shell particle, which most likely corresponds to their dominant distribution within the particle shell. In contrast, the content of iron and nickel is only dominant above the level of the core (with a small overlap to the level of the particle shell).

This result significantly supports the hypothesis of the dominance of a purely metallic phase α(Fe,Ni) within the core. Similar results have been reported from images of nanoparticles collected in an air filling chamber of the InssTek MX-Mini additive manufacturing device by using HAADF-STEM (Noskov et al., 2022). While the crystalline structure of the core (Fig. 1D) represents the metallic phase, the shells crystal structure can only be seen in very small areas on the HRTEM images (Fig. S3). Its approximate *d-space* analysis is in good agreement with the XRD results (Fig. 4) for the crystal structure of chromite ($FeCr_2O_4$).

The EDX microanalysis was also used (Fig. 5) to further refine the model structure of individual nanoparticle components. Due to the problematic precision quantification of the oxygen peak in EDX microanalysis, it is established practice to calculate its stoichiometric ratio in relation to other well-defined elements. When starting from the diffraction model Fig. 4 (αFe - γFe - chromite), the study is limited to the quantitative determination of three dominant metal elements.

The relative percentage fractions of the three dominant metals according to the EDX spectrum from Fig. 5 were determined with a minimum accuracy of approximately 2% (Fe-66 wt%, Ni-12 wt%, Cr-22 wt %). The given values of the individual metal fractions were also verified by elemental analysis (ICP-AES Spectro Arcos). The values of the respective fractions for Fe (378.0 ± 7.6) g/kg, Ni (54.5 ± 2.7) g/kg a Cr (107.0 ± 13.9) g/kg correlate in the 95% confidence interval with the results of the EDX analysis.

3.1. *Formation mechanism theory of studied core-shell nanoparticles*

Kim and Farson (2001) performed model calculations of the interaction between melting laser light and the cloud of emitted metal vapors in approximate axial symmetry. The results of their work show, among other things, the vapor cloud has a plasma character and exhibits significant additional heating by optical absorption. In Fig. 6 a schematic diagram of the plasma cloud with a height of about 0.9 mm over the melting pool is depicted. This diagram was constructed based on the results of modelling during the investigation (Kim and Farson, 2001). The simulation result is also important for understanding the mechanism of formation of the nanoparticles by condensation from the original plasma cloud. According to the simulation, the plasma cloud is dissipated in a characteristic time of about 100 μs after the end of a laser pulse lasting 80 μs. It should be highlighted here that due to the constant lateral argon blowing with a speed of 0.7 ms^{-1}, a characteristic shift of less than 60 μm will occur in 80 μs of irradiation and there is no reason to assume any significant shape deformation of the plasma cloud. Investigating the structure and composition of the emitted solid particles is essential for understanding the mechanism of their formation. Therefore, this analysis was preceded by a characterization of the emitted particles in terms of morphology, chemical composition and crystal structure. Overall, the XRD analysis of the nanopowder clearly confirmed the dominance of the metal phase α(Fe, Ni), which corresponds to kamacite and is in very good agreement with the results of HRTEM *d-space* FFT analysis (Fig. S3).

The remaining question in this situation is the absence of a significant representation of the γ structure on HRTEM images (Fig. 5 and Fig. S2). This apparent problem can be partly explained by the very small difference between the interplanar distances of the assumed α(2.030 Å) and γ(2.060 Å) phases and also by the calculation of both volume fractions in the theoretical model of their core-shell structure, which naturally arises during radial cooling of a melt droplet. Assuming an approximate equality of the densities of the two phases $\rho_\alpha \approx \rho_\gamma$ in calculation (Eq. S4(1)–(3)), the thickness Δr of the shell of phase γ is about 3.9% of the core radius r_α. On the HRTEM images of the core-shell structures, this zone will not be visually apparent, and its volume fraction is less than 10% of the total volume of the metal core. Based on these findings, the existence of a purely metallic core of the core-shell nanoparticles can already be considered as safely proven. It is worthy to note that in the case of arc welding in an argon atmosphere, welding fume

Table 1
The numerical values of d_i (Barthelmy, 2021).

d_1 Å (2θ)	Intensity I_1 (%)	d_2 Å (2θ)	Intensity I_2 (%)	d_3 Å (2θ)	Intensity I_3 (%)	Mineral	Formula
2.0027 (44.67)	100	1.170 (82.35)	30	1.4330 (65.03)	20	Iron	αFe^0
2.030 (44.60)	100	1.976 (46.11)	60	1.435 (64.93)	30	Kamacite	$\alpha Fe^{0+}_{0.9}Ni_{0.1}$
2.060 (43.92)	100	1.780 (51.28)	30	1.260 (75.37)	20	Awaruite	$\gamma(Ni_2Fe - Ni_3Fe)$

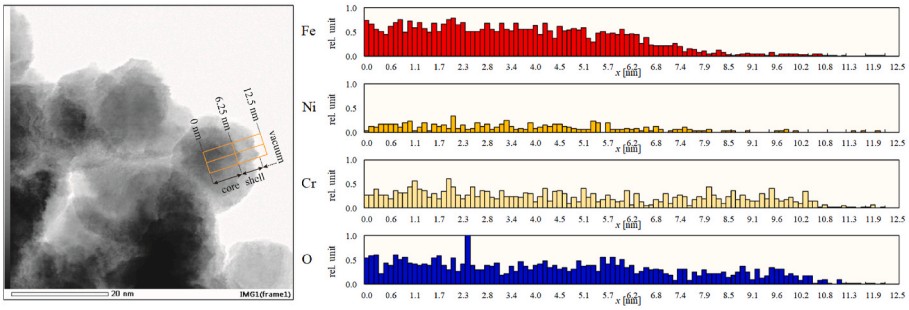

Fig. 3. STEM elemental profiles. (Left) STEM image with marked elemental composition radial axis of the core-shell nanoparticle. Scale bar, 20 nm. **(Right)** Profiles of the presence of the basic elements along the marked radial axis.

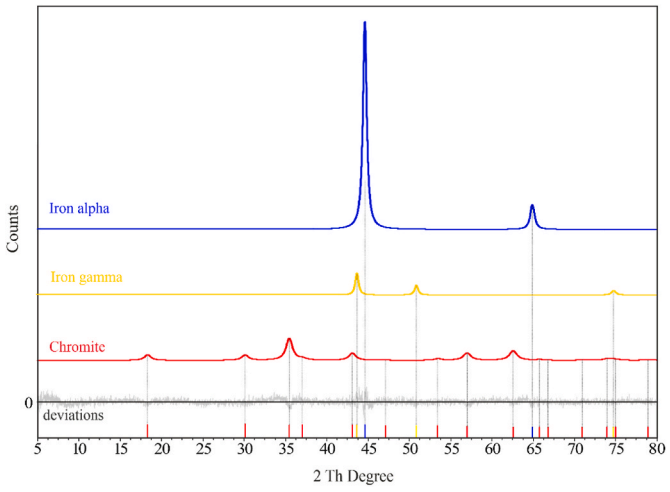

Fig. 4. Phase composition of the newly formed nanomaterial. XRD analysis of aggregated nanostructures confirmed the dominant proportion of the metal phase (α(Fe,Ni) 60 wt%, γ(Fe,Ni) 7 wt%), which is supplemented by 33 wt% of chromite $FeCr_2O_4$. The smaller part of possible substitution by accompanying elements of the primary material (Cr, Mn, Si) does not disturb the original character of the crystalline structure.

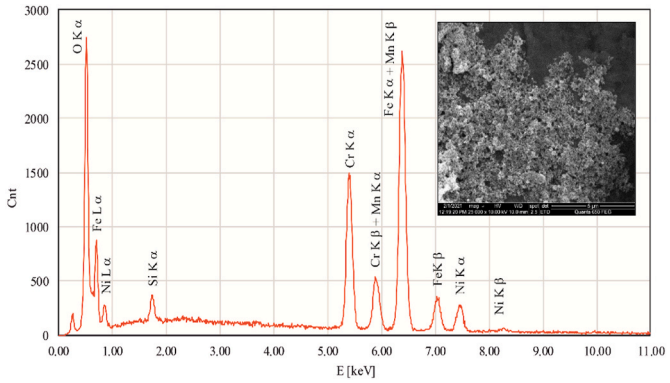

Fig. 5. Elemental composition of the newly formed nanomaterial. Overall EDX spectrum of nanoparticle aggregates. The spectrum was obtained during imaging of a relatively homogeneous nanopowder distributed on area of 5 × 5 μm (inset scale bar, 5 μm).

particles are mostly amorphous oxides in nature and completely different from the particles produced by L-PBF in this case (Berlinger et al., 2011; Jenkins, 2005).

Analysis of the metal/oxide phase ratio (Eq. S5(4)–(18)) shows a disparity between the core/shell ratio determined by HRTEM images

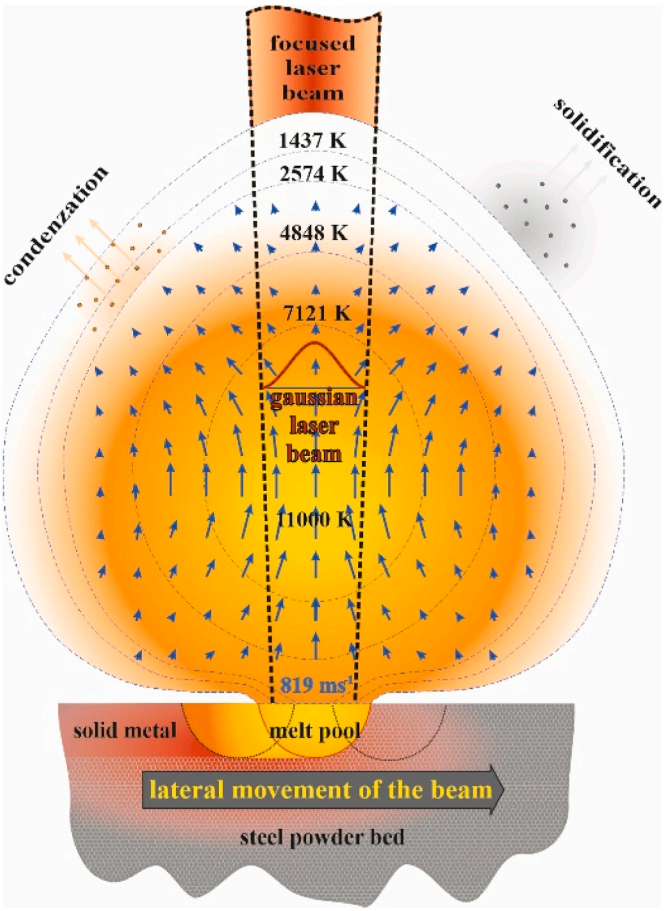

Fig. 6. Scheme of nanoparticles emission condensed over the melting pool.

$[d_{core}/d_{shell}]_{HRTEM}$ = 0.679 and that determined by XRD structural analysis for the hypothetically continuous crystalline chromite phase $[d_{core}/d_{shell}]_{XRD}$ = 0.815. This disproportionation is not matched by any form of chromite, even with a crystalline structure with a high rate of vacancies. The solidification temperature of chromite (about 2200 °C) is significantly higher than that of the metal core. Its presence in the shell provides compelling reasons to adopt a model in which the shell is formed after the inner core is created. Within such a model, the gradual composition of very small nanocrystallites of chromite into a porous granular shell with a higher pore volume can be assumed. The calculated packing factor (0.46) of this granular material (Eq. S4(3)) is approximately comparable to the packing factor (0.52) of a primitive regular cubic sphere arrangement. Under the natural assumption of a certain degree of disorder in the cubic structure, the granular material model shows good agreement with the results obtained by both methods.

Subsequently, from the hypothesis of the relatively accurate determination of two phase components kamacite ($\alpha Fe^{0+}_{0.9}Ni_{0.1}$ – Table 1) and chromite ($FeCr_2O_4$ – Fig. 4), the missing phase $\gamma(Fe_xNi_{1-x})$ will be identified by stoichiometric analysis for the real atomic fractions $X_{Fe} = 0.66$, $X_{Ni} = 0.12$, $X_{Cr} = 0.22$ according to the linear equation (1):

$$\overbrace{[0.9X_{Fe} + 0.1X_{Ni}]}^{\text{kamacite } \alpha Fe_{0.9}Ni_{0.1}} + \overbrace{[(x)X_{Fe} + (1-x)X_{Ni}]}^{\gamma Fe_xNi_{1-x}} + \overbrace{\left[\frac{1}{7}X_{Fe} + \frac{2}{7}X_{Cr} + \frac{4}{7}X_O\right]}^{FeCr_2O_4} = 1 \qquad (1)$$

After substituting the values of real atomic fractions, the linear equation (1) has a stoichiometric root $x \approx 0.24$ and the resulting stoichiometric form of the phase $\gamma Ni_{0.76}Fe_{0.24}$ is closest to the parameters of awaruite γNi_3Fe.

As mentioned above, the volume fraction of this phase is less than 10% of the volume of the whole globular nucleus. The models assumption of the existence of a thin shell of the γNi_3Fe phase above the kamacite core has an exclusively hypothetical character, which can be supported by the argument of a higher surface cooling rate and an observed increase in the nickel content on the surface parts of taenite crystals (Wood, 1967).

An important factor is the discovery of whether the globular nanoparticles were formed simply by explosive spraying of the original stainless steel material or are the result of nucleation and growth from metal vapors above the melting pool. A significant chromium deficiency in the metal core of globular nanoparticles and the extreme surface energy growth with a high degree of fragmentation invalidate the spattering mechanism. If the observed nanoparticles were formed by the solidification of droplets after spraying, the composition of the metal core would essentially be a copy of the ratio (69%Fe):(13%Ni):(18%Cr) of the primary Stainless Steel Powder 316L (DIN 1.4404). For this reason, there is a high probability that there has been nucleation and growth of the nanoparticles from metal vapors above the melting pool. With regard to the residual oxygen content in the argon atmosphere and in the primary material 316L, the chromium deficiency in the metal core may be partially explained by its preferential evaporation and oxidation due to its higher affinity to oxygen compared to the vapors of Fe and Ni (Gasper et al., 2018). This is most likely the cause of the formation of an oxide chromite shell. The globular shape of the metal cores is evidence of the primary vapor → liquid condensation, which corresponds to vapor supersaturation in the region of the respective phase transition. The plasma cloud above the melting pool emits a large amount of charged metal ions, which upon supersaturation of $S \approx 2$ in the condensation region become natural activators of homogeneous nucleation of critical nuclei of size $d \approx 2.2$ nm (Berlinger et al., 2011). Their further growth is realised by the absorption of metal vapors (atoms) falling on the surface of the particle.

With respect to a relatively very short period of thermal pulse, the question is, what is the maximum characteristic growth time of the largest globular nuclei $d = 31$ nm? The stated values of supersaturation and the critical size of the nucleus from previous studies (Berlinger et al., 2011) were used for theoretical analysis of the growth time of the nuclei. Based on the kinetic theory of applications of the Hertz-Knudsen equation, the formula for the dependence of final radius r of the globular metal core on the growth time t was derived (Eq. S5(17)). This model calculation was performed for pure iron (Halstead, 1975), which is thermodynamically similar to kamacite.

The corresponding time dependencies for different values of the supersaturation parameter S are depicted by the graphs in Fig. 7 and confirmed that the growth times are below 200 μs. The above estimated characteristic time of formation of metal cores within the kinetic model is in accordance with the experimentally observed rate of production of particles, which were extracted from the interior walls of the chamber after the end of the 3D printing process. The final globular shape of the core significantly supports the assumption of the existence of a free droplet of molten metal in the solidification phase, without significant deformation by surface artifacts of an oxidic nature. While the solidification of the dominant kamacite occurs in the region of about 1515 °C (Halstead, 1975), the solidification temperature of bulk chromite $FeCr_2O_4$ is about 2400 °C (Swartzendruber et al., 1991). However, even with a more significant decrease of this value due to the Gibbs-Thomson effect, the chromite condensate will solidify into very small nanoparticles at a temperature significantly higher than the solidification temperature of the kamacite core. However, most of the important physicochemical parameters are currently missing to produce a detailed model of their aggregation into the porous shell around the core.

Therefore, only a qualitative assumption of the formation of "nanowelds" on the impact contacts of highly curved surfaces of very small chromite nanoparticles can be made. A similar process occurs in a static mode in some cases of thermal sintering. Within the qualitative sintering model there is not only the primary aggregation of chromite into the shell structure around the core, but also the secondary aggregation of whole core-shell particles into larger aggregates (Fig. 8 - left). Their formation time and mechanical stability were tested by repeated sonication in an ultrasonic field of 35 kHz, 30 W/l for 20 min (Fig. 8 - right). The average deviation recorded in the case of all four measurements was ca. 2%. Under the given conditions without other external influences, the size of the aggregates showed relatively high stability.

3.2. Study of magnetic properties

With regard to the presumed superparamagnetic behavior of the metal cores, a simple magnetization experiment was subsequently performed with a part of the nanopowder. The material was exposed to a magnetic field of 300 mT for 24 h. After 24 h, there was an additional magnetic aggregation of the primary submicron aggregates (Fig. 9) to the size of macroparticles that can be observed by the eye, and their subsequent sedimentation are depicted by the photograph (Fig. 9 inset).

After intensive sonication in a field of 1 kW/l for 20 min, there was a limit dispersion of macroaggregates to a mean size of 970 nm. Regarding the high intensity of the ultrasonic field, it can be stated that the magnetic coupling of the 970 nm limit aggregates was very strong and prevented further dispersion back to the original size. This fact already indicates the presence of a remanent magnetic field, which creates a bond. To compare the time stability of the original material with the magnetized material, a size measurement was performed by the DLS method, lasting about 5 h, and the time evolution of the characteristic diameter d is shown in the graphs (Fig. 8 – right). While the non-magnetized material exhibits excellent time stability with an average uncertainty of 0.4%, the material exposed to the magnetic field reaggregated into larger structures in a relatively short time (Fig. 9), and subsequently sedimented. This behavior is due to the long-range dipole-

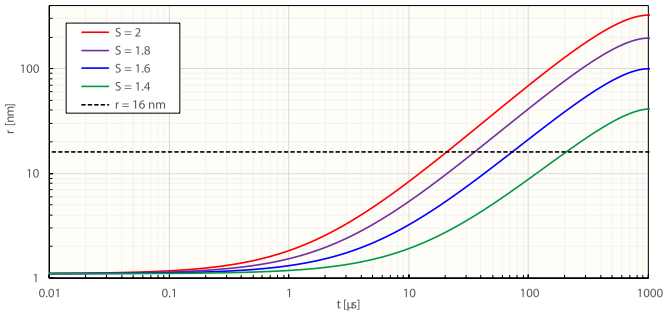

Fig. 7. Theoretical kinetic prediction of metal core growth rate. Dependence of the growth time of a globular metal core on its final radius r, calculated on the basis of a kinetic model (Eq. S5(17)). The conditions correspond to a temperature of 2800 K, and a supersaturation of $S = 2$, 1.8, 1.6 and 1.4. A semiempirical formula for iron, published in (Swartzendruber et al., 1991), was used to approximate the dependence of saturated vapor pressure on temperature $p_{sat}(T)$.

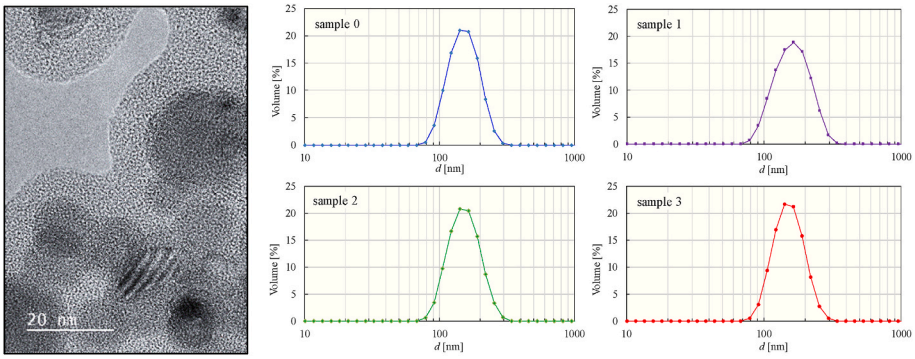

Fig. 8. (Left) Detailed TEM image of globular metal nanoparticles fixed in oxide bonding material. **(Right)** Statistical distributions of the total volume of powder material according to particles sizes were measured in the liquid dispersion (in acetone) by the DLS method. (**Sample 0**) (155 nm) —— 45 days after the first sonication. (**Sample 1**) (166 nm) —— after 20min subsequent sonication. (**Sample 2**) (157 nm) —— after another 20min subsequent sonication. (**Sample 3**) (156 nm) —— after another 20min subsequent sonication.

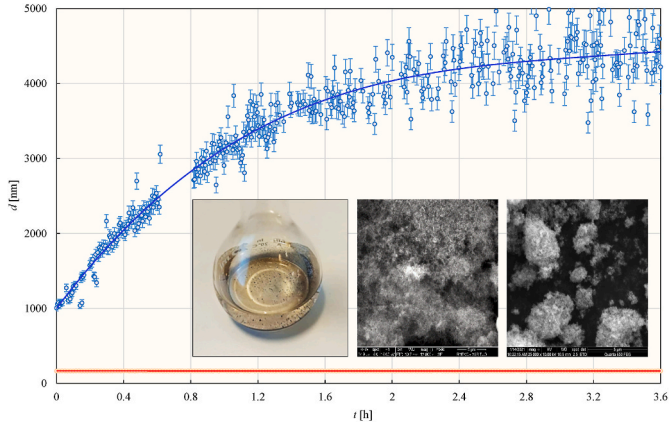

Fig. 9. Comparison of the time evolution of the sizes of the basic nanoparticle aggregates with an original size of about 160 nm. The red curve — shows a constant course with an average uncertainty of 0.4% and corresponds to the nanomaterial without the influence of the magnetic field, the blue curve — shows the time evolution of aggregation after magnetization in the 300 mT field for 24 h (measurement above 3.6 h led to already high reaggregation causing extreme scattering of values outside the permissible limits of the device). (**Inset**) Photograph of magnetically bounded aggregates in acetone and SEM images depicting the condensate nanoparticles without the influence of the magnetic field and on the right their aggregates after the above magnetization. Scale bars, 5 μm. Experimental uncertainties for individual DLS measurements on the Malvern Zetasizer Nano ZS instrument were approximated as simple moving average SMA10 half-width frequency functions of particle size distributions of approximately 4%. (For interpretation of the references to colour in this figure legend, the reader is referred to the Web version of this article.)

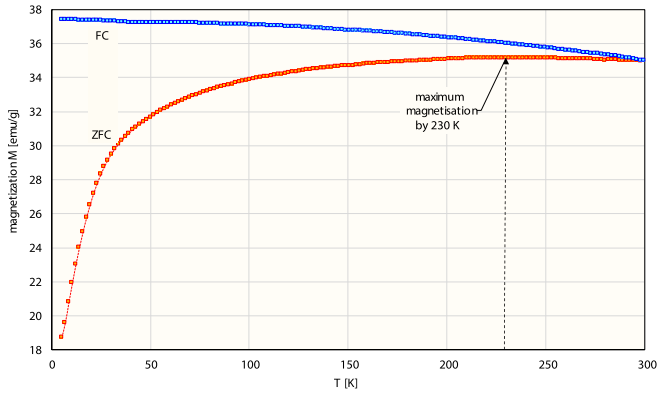

Fig. 10. Magnetic properties of the nanoparticles' system derived from magnetization measurements. Zero-field-cooled (ZFC) and field-cooled (FC) magnetization curves recorded in the temperature interval from 5 to 300 K under intensity of an external magnetic field of 1 kOe. Measurement error bars are not shown because they would be negligibly small (the measurement uncertainty is 5-6 orders of magnitude smaller than the actual measured values for the PPMS DynaCool – Quantum Design measurements).

dipole interaction and provides clear evidence of the presence of a remanent magnetic field within these aggregates.

While the globular nuclei of all core-shell nanoparticles (Fig. 4) have a single-domain character, particles below the superparamagnetic limit $d \approx 14$ nm (Dunlop and Özdemir, 1997; Garrick-Bethell and Weiss, 2010) have a significant part in the statistical distribution on Fig. 2B. Volume fractions under the superparamagnetic limit of the metallic shell is 44%. This means that 56% of the total volume consists of single-domain nanoparticles that can retain remanent magnetization. In order to get a deeper insight into the peculiar magnetic features of this system, zero-field-cooled (ZFC) and field-cooled (FC) magnetization curves were measured (Fig. 10). As seen from ZFC and FC magnetization profiles, the nanoparticles show the clear signs of a thermally activated dynamic magnetic phenomena, typical for analogous magnetic nanosystems (Dormann et al., 2007).

More specifically, the ZFC magnetization curve indicates a gradual unblocking when nanoparticles enter the superparamagnetic regime upon increasing temperature. The unblocking mechanism occurs within a broad temperature window, most probably due to the size distribution of nanoparticles and the evolution of interparticle interactions. This modifies the magnetic anisotropic energy profile of individual magnetic entities when they are assembled. If interparticle interactions are weak (in terms of dipole-dipole interaction), a number of anisotropy minima emerge. This affects the relaxation process of a nanoparticle's superspin within its preferential anisotropy-favored orientations defined by easy axes of magnetization (Dormann et al., 2007).

Due to size distribution and interparticle interactions, the system has a blurred blocking temperature (i.e., a series of blocking temperatures), with a significant portion of nanoparticles still in the magnetically blocked state at room temperature. The existence of interparticle interactions is further documented from the trend of the FC magnetization curve, exhibiting a saturation tendency upon lowering the temperature (Dormann et al., 2007). Thus, it can be concluded that the superparamagnetic relaxation and blocking feature is, to some extent, influenced by magnetic interactions among nanoparticles, of both dipole-dipole and exchange type, most probably with distinct contributions which cannot be clearly distinguished.

More details on the magnetic behavior of the studied system can be deduced from recorded isothermal magnetization curves (Fig. 11). At 5 K, a clear hysteresis is observed, showing evidence for a magnetically blocked regime. The maximum magnetization at 50 kOe (M_{max}(50 kOe, 5 K)) amounts to ~ 66 emu/g, a value implying a relatively strong magnetic response when placed under an external magnetic field. Moreover, the 90% of the M_{max}(50 kOe, 5 K) value is reached under a relatively small field of ~5000 Oe, implying a possibility to drag nanoparticles into the system by a simple hand magnet. The 5 K

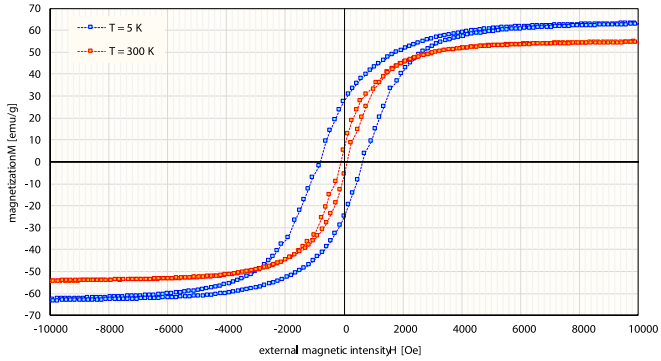

Fig. 11. Magnetic properties of the nanoparticles' system derived from magnetization measurements. Hysteresis loops collected at temperatures of 5 and 300 K under external magnetic fields ranging from – 50 to +50 kOe. Above ±10 kOe the material already shows saturation. Measurement error bars are not shown because they would be negligibly small (the measurement uncertainty is 5-6 orders of magnitude smaller than the actual measured values for the PPMS DynaCool – Quantum Design measurements).

hysteresis loop is shifted with nonidentical values of the positive (H_{c+} (5 K) = 625 Oe) and negative H_{c-} (5 K) = - 805 Oe) coercivity, and positive (M_{r+} (5 K) = 27.6 emu/g) and negative (M_{r-} (5 K) = - 25.0 emu/g) remanent magnetization. This indicates an emergence of an exchange bias phenomenon, a typical manifestation of nanoparticles' systems with a core-shell structure and/or the presence of interparticle magnetic interactions (Iglesias et al., 2008). At 300 K, the hysteresis still persists (H_c = 108.5 Oe and M_r = 6.2 emu/g), indicating that a considerable fraction of nanoparticles is in a magnetically-blocked state with their superspins frozen, within a time window of the magnetization measurement technique (~10 s), along anisotropy-favored directions. This is in agreement with the observations from the measured ZFC/FC magnetization curves and the above-discussed magnetization experiment.

The magnetization measurements, performed under ZFC/FC and isothermal conditions, confirmed both the superparamagnetic state of nanoparticles' nuclei and a magnetically-blocked regime with non-zero remanent magnetization, the portion of which changes with increasing/decreasing temperature. Moreover, the presence of magnetic interparticle interactions was observed, which affect the relaxation time of the superspin in the anisotropy-preferred orientation and the flipping mechanism to another energetically-favored direction.

As already mentioned, interparticle interactions modify the nanoparticle's magnetic anisotropy profile, the extent of which depends on their strength. This alters the character of the superparamagnetic state from a non-interacting case, and eventually leading to a critical collective slow-down of the relaxation phenomenon typical within spin-glass systems. Some authors claim that interparticle interactions promote generation of a self-consistent field (mostly of a dipole-dipole nature) (Leslie-Pelecky and Rieke, 1996). In denser aggregated systems with considerable interparticle interactions and below the percolation limit, superferromagnetism can appear, when individual nanoparticles are viewed as single domains in a continuous network, similar to magnetically-ordered materials (ferromagnets, antiferromagnets, ferrimagnets etc.) (Usov and Serebryakova, 2020).

For bulk materials, remanent magnetization and coercivity are signatures of magnetic ordering. However, for a single-domain nanoparticle, non-zero values of remanent magnetization and coercivity can also be observed and understood within the concept of the Stoner-Wohlfarth model (Bedanta and Kleemann, 2009). Here, it should be stressed that the size of a nanoparticle must lie within the interval determined by a superparamagnetic limit (lower limit) and the transition from a single-domain state to a multi-domain regime (upper limit) (Fig. 12) (Bedanta and Kleemann, 2009). Thus, if the size of the

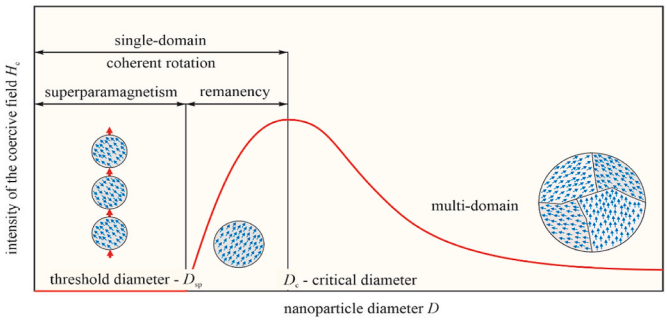

Fig. 12. Dependence of coercivity (H_c) on particle size (D) for ultrafine nanoparticles. Critical diameter D_c denotes the transition from the single-domain to multi-domain state and D_{sp} stands for the superparamagnetic limit.

nanoparticle falls within this range, it shows remanent magnetization and coercivity, the values of which depend on the instant orientation of the nanoparticle's superspin along a particular anisotropy axis and the direction of the external magnetic field. Moreover, as clearly seen from the asymmetric profile of the low-temperature hysteresis loop, the system experiences an exchange bias (Iglesias et al., 2008).

Its evolution is, most probably, connected with a core-shell architecture of the nanoparticles with different magnetic regimes shown by the nanoparticle's core and shell. Here, it can be hypothesized that based on the identified chemistry of the nanoparticles, the core is most probably perfectly ferromagnetically-ordered while the shell might show a ferrimagnetic (or some canted) structure. Thus, the magnetic features of the nanoparticles' system are governed by several magnetic effects. Some are expected to play a more significant role than others, while synergy among them cannot be excluded. It is very difficult to experimentally evaluate their specific contributions.

Thus, it can be concluded that the observed magnetic behavior (i.e., non-zero remanent magnetization, coercivity) is a consequence of nanoparticles in a magnetically-blocked state and with their size being above the superparamagnetic limit. Moreover, the effect of exchange bias and interparticle interactions (generation of a self-consistent field and potential superferromagnism) can promote and maintain extra "magnetic ordering" within the nanoparticles' system, contributing to some extent, to its magnetic response.

4. Application of findings in additive manufacturing

This newly acquired information about the magnetic properties of the nanoparticles produced during the LPBF process can potentially be used by 3D printer manufacturers to prevent the release of potentially harmful nanoparticle emissions into the indoor environment through magnetic separation. Moreover, this observation of the specific superparamagnetic behavior of emitted nanoparticles could be used to magnetically remove them before they reach the commonly used paper filters. This can lead to enhanced filter life and reduction of emissions/reduction of operating costs and environmental disposal costs. The reduction of potentially harmful emissions is worth of further research and development of a magnetic separator, which must be part of the design of the 3D printer, placed in front of the filter vessel. This magnetic separator separates the metal particles that clog the filtration device. This solution will extend the durability and lifetime of the filter, which has a positive impact on material management, the environmental disposal of the filtration equipment, and an overall positive impact on a cleaner and more sustainable production process.

It is also known that one of the most dangerous substances within the LPBF process is the nanoparticle condensate, which is formed by the evaporation of liquid metal and condensation in the form of fine particles with a high surface area, which are captured in the filter, making filter replacement the most dangerous part of 3D printer operation

(DebRoy et al., 2019; Hu et al., 2020).

The method outlined in this study could remove this hazard by removing the nanoparticles before they reach the filter by using simple magnetic separators. Considering the likely increase in use of 3D printing using stainless steel, this magnetic separation may significantly reduce occupational health risks caused by emitted particles.

The magnetic properties of these nanoparticles could also be of vital importance for potential applications especially in fields where a relatively large magnetic response of a material is required under a small external magnetic field (e.g., sensors). Due to the fact that the studied nanoparticles are a by-product of the LPBF process, these could be recycled for use within other manufactoring sectors.

The approach used to solve the problem of formation and emission of condensates from metal evaporation over a laser melt pool is based on three basic factors.

1) Physico-chemical conditions of the process model: atoms/clusters of Fe, Ni and Cr metal vapors are emitted from the surface of the laser melt pool at temperatures where total plasmaisation does not occur and are cooled by expansion and convective diffusion in ambient slow flowing Argon 5.0 (purity $\geq$99.999%) with a pressure of 13 mbar and with an O_2 content <2 ppm and H_2O < 2 ppm.
2) Experimental basis of the process study: the solidified metal aerosol particles in the chamber were extracted by wiping and then separated from the microparticles of the primary material by sedimentation. Afterwards, their comprehensive characterization was carried out, necessary to confront them with the theoretical model.
3) Theoretical physicochemical model of the process: the model was based on a very general thermodynamic analysis of the phase transition "metal vapor → solid particle" with minimal influence of plasmaization on the expending vapors.

The confrontation of the theoretical model with experimental data demonstrated its realistic character, which will be used in the future to model the local magnetic separation of aerosols in the vicinity of the laser melt pool, taking into account the spatial zone of transition through the Curie point.

The only realistic limitation of the above study is the specific conditions of factor 1) above. However, since the conditions in the laser printing chambers tend to be very similar, this is not a significant model limitation in this application area of 3D printing.

5. Conclusions

This detailed study reports the creation of superparamagnetic core-shell nanoparticles proposed kinetic model for their formation above a laser melting pool during the 3D printing of stainless steel using LPBF. Experimental data indicates the presence of core-shell nanoparticles with a mean size of 14 nm within a size range of 3–36 nm. Larger individual nanoparticles in the studied samples were not observed. The HRTEM image analysis revealed a relatively high degree of correlation of the linear dependence between the diameter of the core-shell nanoparticle and the diameter of its core. Quantitative linear (STEM) elemental analysis used in this study, contrary to commonly used elemental point mapping, provided more detailed information on the representation of individual elements on the radial core-shell nanoparticle and confirmed the metallic character of the core. It was found that the core structure is metallic with a distinct monocrystalline character (consisting of kamacite, which is usually found in meteorites), while the shell consists of a heterogeneous chromite structure; the crystalline structure of the metal core was clearly demonstrated by both *d*-space and XRD analysis. The proven absence of stoichiometric chromium in the core proves that these are not particles formed by spattering of the primary stainless steel material. The newly proposed kinetic model based on experimental data for the studied LPBF process predicted the metal core growth time to be below 200 μs, which is consistent with the observed dimensions of the particles produced under the given conditions. Magnetic measurements of the newly formed nanomaterial proved the complete dominance of single-domain cores of ferromagnetic material, a large part of which are nanoparticles below the superparamagnetic threshold. The asymmetry in the magnetic hysteresis confirmed the core-shell interaction in the core-shell structure and also the core-shell interaction in the multiparticle composite aggregates, which may partially manifest in the form of superferromagnetism.

The results of the study demonstrated the superparamagnetic nature of the condensate nanoparticles. Due to the very small volume of the nanoparticles, the cooling process in the inert atmosphere down to below the Curie point of 760 °C is very fast, and the particles can interact with the magnetic field already in the vicinity of the laser melt pool. This fact directly enables efficient magnetic separation of this dense aerosol in the nearby vicinity of tens of cm. This local separation could eliminate the environmental risk of surface contamination of the inner surface of the working chamber, prolong the lifetime of the air filters at the chamber outlet and decrease contamination of raw materials with the newly formed oxidic phase, which may adversely affect the quality of the printed metal parts.

Moreover, these findings are also very important for a new technological approach for the targeted preparation of globular core-shell superparamagnetic nanoparticles with kamacite metal core in laser powder bed fusion of austenitic steel 316L powder. Further research in this area will lead to testing the magnetic separator and studying the effect of removing these unwanted intermediates on the properties of the final metal products and the condition of the filter components in the 3D printer used.

Availability of data and material

The authors confirm that the data supporting the findings of this study are available within the article and its supplementary materials.

CRediT authorship contribution statement

Richard Dvorsky: Writing - Original Draft, Writing - Review & Editing, Data Curation, Conceptualization, Investigation, Methodology, Formal analysis, Funding acquisition, Supervision, Validation. **Jana Kukutschova:** Writing - Original Draft, Writing - Review & Editing, Conceptualization, Funding acquisition, Supervision. **Marek Pagáč:** Writing - Original Draft, Writing - Review & Editing, Resources, Investigation, Methodology, Funding acquisition, Supervision. **Ladislav Svoboda:** Writing - Original Draft, Writing - Review & Editing, Data Curation, Investigation, Funding acquisition, Supervision. **Zuzana Šimonová:** Investigation. **Kateřina Peterek Dědková:** Investigation. **Jiří Bednář:** Writing - Original Draft, Writing - Review & Editing, Formal analysis. **Rafael Gregorio Mendes:** Investigation. **Dalibor Matýsek:** Investigation. **Ondřej Malina:** Writing - Original Draft, Writing - Review & Editing, Investigation, Methodology, Funding acquisition, Formal analysis, Validation. **Jiří Tuček:** Writing - Original Draft, Writing - Review & Editing, Investigation, Methodology, Formal analysis. **Zuzana Vilamová:** Investigation. **Sergei Kiselev:** Investigation. **Thomas Gemming:** Investigation. **Peter Filip:** Conceptualization.

Declaration of competing interest

The authors declare that they have no known competing financial interests or personal relationships that could have appeared to influence the work reported in this paper.

Data availability

Data will be made available on request.

Acknowledgements

We thank J. Seidlerová for ICP measurements and M. Cieslar for help during TEM and STEM analyses. This work was supported by Structural Funds of European Union project "Innovative and additive manufacturing technology - new technological solutions for 3D printing of metals and composite materials," (CZ.02.1.01/0.0/0.0/17_049/0008407), by Gamma PP1 (TP01010036) by Technology Agency of the Czech Republic, by DGS/TEAM/2020-001 "Organic and inorganic pathogenic nanoparticles and the formation of appropriate protective barriers based on electroactive nanomaterials" funded by Operational Programme Research, Development and Education (CZ.02.2.69/0.0/0.0/19_073/0016945), by European Regional Development Fund in the IT4Innovations national supercomputing center - path to exascale project (EF16_013/0001791), by Operational Programme Research, Development and Education financed by the EU and from the budget of the Czech Republic "Innovative therapeutic methods of musculoskeletal system in accident surgery" (CZ.02.1.01/0.0/0.0/17_049/0008441) and by the student project SP2023/095 of VSB-Technical University of Ostrava. O.M. would like to thank to the following projects: the Research Infrastructure NanoEnviCz, supported by the Ministry of Education, Youth and Sports of the Czech Republic under Project No. LM2018124 and the ERDF/ESF project "Nano4Future" (No. CZ.02.1.01/0.0/0.0/16_019/0000754) of the Ministry of Education, Youth and Sports of the Czech Republic.

Appendix A. Supplementary data

Supplementary data to this article can be found online at https://doi.org/10.1016/j.jclepro.2023.136688.

References

Barthelmy, D., 2021. Mineralogy database [WWW document]. http://webmineral.com/.
Bedanta, S., Kleemann, W., 2009. Supermagnetism. J. Phys. D Appl. Phys. 42, 013001 https://doi.org/10.1088/0022-3727/42/1/013001.
Berlinger, B., Benker, N., Weinbruch, S., LVov, B., Ebert, M., Koch, W., Ellingsen, D.G., Thomassen, Y., 2011. Physicochemical characterisation of different welding aerosols. Anal. Bioanal. Chem. 399, 1773–1780. https://doi.org/10.1007/s00216-010-4185-7.
Böckin, D., Tillman, A.-M., 2019. Environmental assessment of additive manufacturing in the automotive industry. J. Clean. Prod. 226, 977–987. https://doi.org/10.1016/j.jclepro.2019.04.086.
Calignano, F., Manfredi, D., Ambrosio, E.P., Biamino, S., Lombardi, M., Atzeni, E., Salmi, A., Minetola, P., Iuliano, L., Fino, P., 2017. Overview on Additive Manufacturing Technologies. Proc. IEEE 105, 593–612. https://doi.org/10.1109/JPROC.2016.2625098.
Chen, R., Yin, H., Cole, I.S., Shen, S., Zhou, X., Wang, Y., Tang, S., 2020. Exposure, assessment and health hazards of particulate matter in metal additive manufacturing: a review. Chemosphere 259 (127452). https://doi.org/10.1016/j.chemosphere.2020.127452.
DebRoy, T., Mukherjee, T., Milewski, J.O., Elmer, J.W., Ribic, B., Blecher, J.J., Zhang, W., 2019. Scientific, technological and economic issues in metal printing and their solutions. Nat. Mater. 18, 1026–1032. https://doi.org/10.1038/s41563-019-0408-2.
Dormann, J.L., Fiorani, D., Tronc, E., 2007. Magnetic relaxation in fine-particle systems. Pp. 283–494. https://doi.org/10.1002/9780470141571.ch4.
Dunlop, D.J., Özdemir, Ö., 1997. Rock Magnetism. Cambridge University Press. https://doi.org/10.1017/CBO9780511612794.
Garrick-Bethell, I., Weiss, B.P., 2010. Kamacite blocking temperatures and applications to lunar magnetism. Earth Planet Sci. Lett. 294, 1–7. https://doi.org/10.1016/j.epsl.2010.02.013.
Gasper, A.N.D., Szost, B., Wang, X., Johns, D., Sharma, S., Clare, A.T., Ashcroft, I.A., 2018. Spatter and oxide formation in laser powder bed fusion of Inconel 718. Addit. Manuf. 24, 446–456. https://doi.org/10.1016/j.addma.2018.09.032.
Halstead, W.D., 1975. A review of saturated vapour pressures and allied data for the principal corrosion products of iron, chromium, nickel and cobalt in flue gases. Corrosion Sci. 15, 603–625. https://doi.org/10.1016/0010-938X(75)90027-X.
Harun, W.S.W., Kamariah, M.S.I.N., Muhamad, N., Ghani, S.A.C., Ahmad, F., Mohamed, Z., 2018. A review of powder additive manufacturing processes for metallic biomaterials. Powder Technol. 327, 128–151. https://doi.org/10.1016/j.powtec.2017.12.058.
Hu, X., Takada, N., Machmudah, S., Wahyudiono, Kanda, H., Goto, M., 2020. Ultrasonic-enhanced fabrication of metal nanoparticles by laser ablation in liquid. Ind. Eng. Chem. Res. 59, 7512–7519. https://doi.org/10.1021/acs.iecr.9b06384.
Huang, R., Riddle, M., Graziano, D., Warren, J., Das, S., Nimbalkar, S., Cresko, J., Masanet, E., 2016. Energy and emissions saving potential of additive manufacturing: the case of lightweight aircraft components. J. Clean. Prod. 135, 1559–1570. https://doi.org/10.1016/j.jclepro.2015.04.109.
Iglesias, O., Labarta, A., Batlle, X., 2008. Exchange bias phenomenology and models of core/shell nanoparticles. J. Nanosci. Nanotechnol. 8, 2761–2780.
Jenkins, N.T.E.T.W., 2005. Chemical analysis of welding fume particles. Weld. Journal-NEW YORK- 84, 87–93.
Kanyilmaz, A., Demir, A.G., Chierici, M., Berto, F., Gardner, L., Kandukuri, S.Y., Kassabian, P., Kinoshita, T., Laurenti, A., Paoletti, duPlessis, I., Razavi, A., S, M.J., 2022. Role of metal 3D printing to increase quality and resource-efficiency in the construction sector. Addit. Manuf. 50, 102541 https://doi.org/10.1016/j.addma.2021.102541.
Kim, K.R., Farson, D.F., 2001. CO2 laser–plume interaction in materials processing. J. Appl. Phys. 89, 681–688. https://doi.org/10.1063/1.1329668.
Ko, H.S., Jeong, S.Bin, Phyo, S., Lee, J., Jung, J.H., 2021. Emission of particulate and gaseous pollutants from household laser processing machine. J. Environ. Sci. 103, 148–156. https://doi.org/10.1016/j.jes.2020.10.018.
Leslie-Pelecky, D.L., Rieke, R.D., 1996. Magnetic properties of nanostructured materials. Chem. Mater. 8, 1770–1783. https://doi.org/10.1021/cm960077f.
Lin, L., Kollipara, P.S., Zheng, Y., 2019. Digital manufacturing of advanced materials: challenges and perspective. Mater. Today 28, 49–62. https://doi.org/10.1016/j.mattod.2019.05.022.
Liu, J., Gaynor, A.T., Chen, S., Kang, Z., Suresh, K., Takezawa, A., Li, L., Kato, J., Tang, J., Wang, C.C.L., Cheng, L., Liang, X., To, A.C., 2018. Current and future trends in topology optimization for additive manufacturing. Struct. Multidiscip. Optim. 57, 2457–2483. https://doi.org/10.1007/s00158-018-1994-3.
Murzin, S.P., 2022. Improvement of thermochemical processes of laser-matter interaction and optical systems for wavefront shaping. Appl. Sci. 12, 12133 https://doi.org/10.3390/app122312133.
Noskov, A., El-Khoury, M., Drobyshev, S., Kuchaev, E., Yanbaev, F., Zhigalina, O., Khmelenin, D., Gilmutdinov, A., 2022. A microscopy study of nanoparticles emitted during laser additive manufacturing with stainless steel powder. Mater. Lett. X 14 (100139). https://doi.org/10.1016/j.mlblux.2022.100139.
Noskov, A., Ervik, T.K., Tsivilskiy, I., Gilmutdinov, A., Thomassen, Y., 2020. Characterization of ultrafine particles emitted during laser-based additive manufacturing of metal parts. Sci. Rep. 10 (20989) https://doi.org/10.1038/s41598-020-78073-z.
RENISHAW, 2018. SS 316L-0407 powder for additive manufacturing [WWW Document]. http://resources.renishaw.com/en/download/data-sheet-ss-316l-0407-powder-for-additive-manufacturing-90802.
Sun, C., Wang, Y., McMurtrey, M.D., Jerred, N.D., Liou, F., Li, J., 2021. Additive manufacturing for energy: a review. Appl. Energy 282, 116041. https://doi.org/10.1016/j.apenergy.2020.116041.
Swartzendruber, L.J., Itkin, V.P., Alcock, C.B., 1991. The Fe-Ni (iron-nickel) system. J. Phase Equil. 12, 288–312. https://doi.org/10.1007/BF02649918.
Torres-Carrillo, S., Siller, H.R., Vila, C., López, C., Rodríguez, C.A., 2020. Environmental analysis of selective laser melting in the manufacturing of aeronautical turbine blades. J. Clean. Prod. 246 (119068) https://doi.org/10.1016/j.jclepro.2019.119068.
Usov, N.A., Serebryakova, O.N., 2020. Equilibrium properties of assembly of interacting superparamagnetic nanoparticles. Sci. Rep. 10 (13677) https://doi.org/10.1038/s41598-020-70711-w.
Wang, Y.M., Voisin, T., McKeown, J.T., Ye, J., Calta, N.P., Li, Z., Zeng, Z., Zhang, Y., Chen, W., Roehling, T.T., Ott, R.T., Santala, M.K., Depond, P.J., Matthews, M.J., Hamza, A.V., Zhu, T., 2018. Additively manufactured hierarchical stainless steels with high strength and ductility. Nat. Mater. 17, 63–71. https://doi.org/10.1038/nmat5021.
Wood, J.A., 1967. Chondrites: their metallic minerals, thermal histories, and parent planets. Icarus 6, 1–49. https://doi.org/10.1016/0019-1035(67)90002-4.
Wu, H., Mehrabi, H., Karagiannidis, P., Naveed, N., 2022. Additive manufacturing of recycled plastics: strategies towards a more sustainable future. J. Clean. Prod. 335 (130236) https://doi.org/10.1016/j.jclepro.2021.130236.